WATER RESOURCES RESEARCH, VOL. 49, 7575–7586, doi:10.1002/2013WR013667, 2013

Effects of network dissolution changes on pore-to-core upscaled reaction rates for kaolinite and anorthite reactions under acidic conditions

Daesang Kim[1] and W. Brent Lindquist[2]

Received 7 February 2013; revised 15 August 2013; accepted 25 October 2013; published 20 November 2013.

[1] We have extended reactive flow simulation in pore-network models to include geometric changes in the medium from dissolution effects. These effects include changes in pore volume and reactive surface area, as well as topological changes that open new connections. The computed changes were based upon a mineral map from an X-ray computed tomography image of a sandstone core. We studied the effect of these changes on upscaled (pore-scale to core-scale) reaction rates and compared against the predictions of a continuum model. Specifically, we modeled anorthite and kaolinite reactions under acidic flow conditions during which the anorthite reactions remain far from equilibrium (dissolution only), while the kaolinite reactions can be near-equilibrium. Under dissolution changes, core-scale reaction rates continuously and nonlinearly evolved in time. At higher injection rates, agreement with predictions of the continuum model degraded significantly. For the far-from-equilibrium reaction, our results indicate that the ability to correctly capture the heterogeneity in dissolution changes in the reactive mineral surface area is critical to accurately predict upscaled reaction rates. For the near-equilibrium reaction, the ability to correctly capture the heterogeneity in the saturation state remains critical. Inclusion of a Nernst-Planck term to ensure neutral ionic currents under differential diffusion resulted in at most a 9% correction in upscaled rates.

Citation: Kim, D., and W. B. Lindquist (2013), Effects of network dissolution changes on pore-to-core upscaled reaction rates for kaolinite and anorthite reactions under acidic conditions, *Water Resour. Res.*, *49*, 7575–7586, doi:10.1002/2013WR013667.

1. Introduction

[2] A series of papers [*Kim and Lindquist*, 2011; *Kim et al*., 2011; *Li et al*., 2006, 2007] have developed reactive network-flow model simulation for computing upscaled reaction rates at the core scale. The development of the network-flow model has included: convection and diffusion of dissolved species, with kinetic modeling of mineral surface reactions and instantaneous equilibrium modeling of aqueous reactions [*Li et al*., 2006]; investigation of the influence of the spatial distribution of mineral species in media that are theoretical [*Li et al*., 2007] and mapped from real samples [*Kim et al*., 2011]; and investigation of dependence on kinetic rate laws and on bulk flow rate [*Kim and Lindquist*, 2011]. While the methodology is general, the specific application has been the study of anorthite and kaolinite dissolution and precipitation as model reactions that may occur during CO_2 sequestration in sandstone basins. These simulations were performed in networks extracted from 3-D images of basin sandstones. The network matrix was modeled as composed of quartz, anorthite and kaolinite grains. The underlying importance of this work is that the laboratory measured reaction rates, typically developed in batch reactors under homogeneous conditions, do not predict the bulk rates seen in porous media where heterogeneities in mineral distribution, flow rate, and geometry have strong effects [*Kim and Lindquist*, 2011; *Kim et al*., 2011]. One critique of the methodology to date is that the underlying network-flow model computations have neglected the geometrical effects that accompany dissolution and precipitation processes [*Kim et al*., 2011]. A second critique, which we note here for the first time, is the lack of inclusion of a Nernst-Planck (N-P) term in the governing transport equations to ensure the absence of an electric current as species of different charges diffuse at different rates. We address both of these deficiencies in our reactive pore-network model in this paper.

[3] Under the acidic conditions of our study, anorthite grains dissolve while kaolinite either dissolves or precipitates depending on local pore conditions [*Kim and Lindquist*, 2011; *Kim et al*., 2011], and quartz grains do not react. Our previous work, corroborated by the computations performed here, indicated that the bulk rate of anorthite mass transfer (mol s^{-1}) from reaction was at least 200 times faster than that for kaolinite. Under these conditions the accessible anorthite dissolved completely from the matrix before significant kaolinite mass changes occurred. As a consequence, we have modeled only the geometric changes accompanying anorthite dissolution in the

[1]Clean Combustion Research Center, King Abdullah University of Science and Technology, Thuwal, Saudi Arabia.
[2]Department of Applied Mathematics and Statistics, Stony Brook University, Stony Brook, New York, USA.

Corresponding author: W. B. Lindquist, Department of Applied Mathematics and Statistics, Stony Brook University, Stony Brook, NY 11794-3600, USA. (lindquis@ams.sunysb.edu)

0043-1397/13/10.1002/2013WR013667

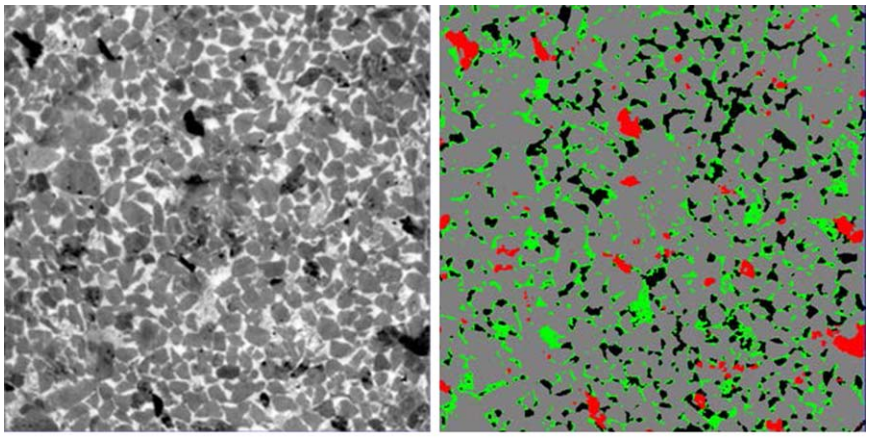

Figure 1. (a) One slice from the XCMT image of sandstone sample 3W4. The slice size is 2.9 mm × 2.9 mm. Voxel size is 3.98 μm. (b) The segmented image of this slice showing the four-phase mapping input into the network model: black, void space; green, authigenic clays (assumed kaolinite); grey, quartz; red, allogenic grains (assumed anorthite).

simulations presented here. We model dissolution by a uniform depth erosion of anorthite grain surfaces. During dissolution, appropriate exposed anorthite grain surfaces erode, affected pore volumes increase, and affected channel cross-sectional areas grow. We also show that sufficient erosion of anorthite grains will lead to the creation of new channels in the network.

[4] Inclusion of Nernst-Planck diffusion terms in the system of transport equations for aqueous species necessitates dealing with terms that are nonlinear and coupled in the concentrations of all chemical species, especially when the system of transport equations is reduced to that for total concentrations and solved implicitly [*Liu et al*., 2011]. We suggest an approach that simplifies the evaluation of the Nernst-Planck terms at the cost of a larger set of transport equations.

[5] For a sandstone network developed from a 3-D X-ray computed tomography (XCMT) image, we computed the bulk (core-scale) reaction rate, allowing for geometric changes in the network resulting from dissolution of anorthite grains under acidic fluid conditions compatible with CO_2 sequestration. We compared the upscaled rates computed with and without the Nernst-Planck term. In addition, we compared these network rates against those computed by a continuum formulation.

2. Materials and Methods

2.1. The Pore-Network Model

[6] Using XCMT and the 3DMA-Rock software package [*Lindquist et al*., 2000; *Oh and Lindquist*, 1999; *Shin et al*., 2005], a pore-network model was constructed from a core sample (3W4) extracted from the Viking formation in the Alberta Basin. The network had size 2.9 × 2.9 × 1.4 mm^3. The pore-network description, extracted from the XCMT image (voxel size 3.98 μm), included pore position and volume, throat perimeter and area, channel length, and pore-pore connectivity. Details on the pore network (distributions on pore size, throat size, coordination number, and channel length) are provided in *Kim et al*. [2011].

[7] An important component of the network model was developed by partitioning computed tomography (CT) values into void space, quartz, minerals with CT values less than that of quartz, and minerals with CT values greater than that of quartz. Based upon independent analyses [*Peters*, 2009], we inferred that the minerals with CT values less than that of quartz were primarily authigenic clay minerals (largely kaolinite), while those with CT values greater than that of quartz were primarily allogenic minerals, including the presence of anorthite. In the network modeling studies, we assumed that all the clay minerals were kaolinite and all allogenic minerals were anorthite. Thus, as illustrated in Figure 1, we achieved a reasonably realistic 3-D map of kaolinite and anorthite mineral distribution throughout the sample. In particular, using the pore network extracted by 3DMA-Rock together with the marching cubes algorithm [*Lorensen and Cline*, 1987] on the void and mineral phase segmented images, we were able to compute the flow-accessible surface areas of the quartz, kaolinite, and anorthite minerals in each pore. The distributions of kaolinite and anorthite surface area are also given in *Kim et al*. [2011].

2.2. Model for Geometrical Change With Anorthite Dissolution

[8] Using the mathematical morphology erosion technique [*Serra*, 1982], 3DMA-Rock can digitally erode any anorthite grain, voxel-layer by voxel-layer, starting from the pore-exposed voxel faces. This erosion expands pores, changes the exposed anorthite surface areas, and generates geometric changes, such as extension of throat surfaces (Figure 2), and the creation of new pore-pore connections changes (Figure 3).

[9] Consider the two pores, *i* and *j*, shown in Figure 2. This is a 2-D illustration of the detail of the 3-D digitized map that would be generated for such a pair of pores. Included in this illustration is the throat surface, t_{ij}^0,

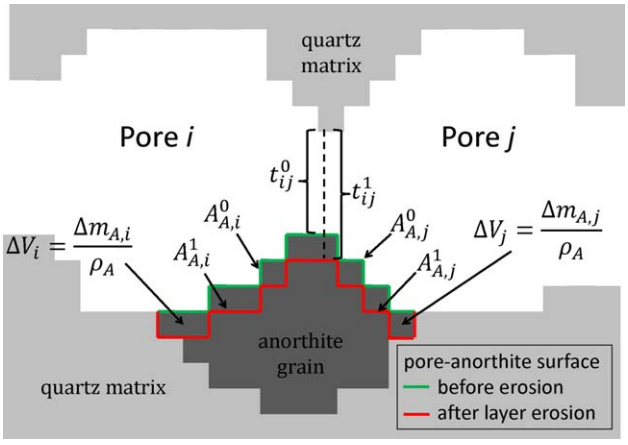

Figure 2. The 2-D illustration of a uniform, six-connected, single-voxel-layer erosion of an anorthite grain surface showing the geometrical changes in anorthite surface area, $A_{A,i}^0 \rightarrow A_{A,i}^1$ and $A_{A,j}^0 \rightarrow A_{A,j}^1$, pore volume, ΔV_i and ΔV_j, and anorthite mass, $\Delta m_{A,i}$ and $\Delta m_{A,j}$, in pores i and j, as well as the change in throat area, $t_{ij}^0 \rightarrow t_{ij}^1$, in the connecting channel; ρ_A is the density of anorthite.

computed between the two pores and an anorthite grain embedded in the quartz matrix. The anorthite grain forms part of the surface area of the two pores. A single-layer, six-connected digitized erosion of the anorthite grain is demonstrated in Figure 2, indicating the changed anorthite surface areas $A_{A,i}^0 \rightarrow A_{A,i}^1$ and $A_{A,j}^0 \rightarrow A_{A,j}^1$ induced in each pore. The changes in pore volume, ΔV_i and ΔV_j, and the corresponding mass changes, $\Delta m_{A,i}$ and $\Delta m_{A,j}$, induced in each pore resulting from this eroded layer are also indicated in Figure 2. Such a digitized erosion process was performed by the 3DMA-Rock software package, layer by layer, until each anorthite grain was completely eroded. Relevant details on the geometric changes were stored in tables organized for each pore (changes in pore volume, anorthite surface area, dissolved anorthite mass) and for each pore-pore connection (changes in throat area, shape factor, channel length) as a function of erosion layer number.

[10] Figure 3 demonstrates how erosion of an anorthite grain can lead to new pore-pore connections. Pores i and j are separated by cemented quartz-anorthite grains (Figure 3a). Partial dissolution of the anorthite grain opens up a channel between the two pores (Figure 3b). Such new pore-pore connections were flagged as local topological changes [*Lee et al*., 1994] in the grain space during the layer-by-layer digital erosion of anorthite grain surfaces. These new pore-pore connections, with appropriate information on eroded anorthite mass, throat area, shape factor, and channel length were added to the erosion layer tables. Such new connections entered into the numerical simulations only when the local anorthite mass changes reached the appropriate threshold values indicated by the appropriate pore table.

[11] The erosion layer tables discussed earlier quantified geometrical changes based upon voxel-based erosion layers. With a voxel resolution of 3.98 μm, these erosion layers produced mass changes that were much greater than mass changes produced by anorthite dissolution over a single numerical time step in the reaction simulations. In each time step the numerical simulations calculated a dissolved anorthite mass from each pore surface. Values in the appropriate pore and channel lookup tables were therefore linearly interpolated to produce the appropriate values of pore and pore-connection geometrical changes accompanying the calculated mass changes.

2.3. The Reactive Transport Model

[12] Reactive transport of N_S chemical species is governed by the standard mass conservation system of equations describing advection, diffusion, and reactive change in species concentrations [α],

$$\frac{\partial[\alpha]}{\partial t} + v \cdot \nabla[\alpha] = \nabla \cdot \sum_{\beta=1}^{N_S} D_{\alpha\beta} \nabla[\beta] + s_\alpha, \quad \alpha = 1, \ldots, N_S, \tag{1}$$

where v is the flow velocity and s_α is the net concentration production rate for species α from reaction. The diffusion term, $D_{\alpha\beta}$, has the form [*Liu et al*., 2011]

$$D_{\alpha\beta} = \left(D_\alpha \delta_{\alpha\beta} - \frac{z_\alpha z_\beta D_\alpha D_\beta [\alpha]}{\sum_{\lambda=1}^{N_s} z_\lambda^2 D_\lambda [\lambda]} \right), \tag{2}$$

where D_α is the diffusion coefficient for, and z_α is the charge of, species α and $\delta_{\alpha\beta}$ is the Kronecker δ function. The last term in (2) is the Nernst-Planck charge induced flux required to maintain zero electrical current under differential diffusion speeds of differently charged ionic species.

[13] System (1) is formulated for individual species and requires knowledge of rates for fast reactions that are usually treated as (instantaneous) equilibrium reactions and for slow reactions usually represented by kinetic terms. To eliminate the need for fast reaction rates, which are typically not available, the chemical species can be divided into two sets: N_I independent species and N_D dependent species, where $N_I + N_D = N_S$. Each species in the latter set

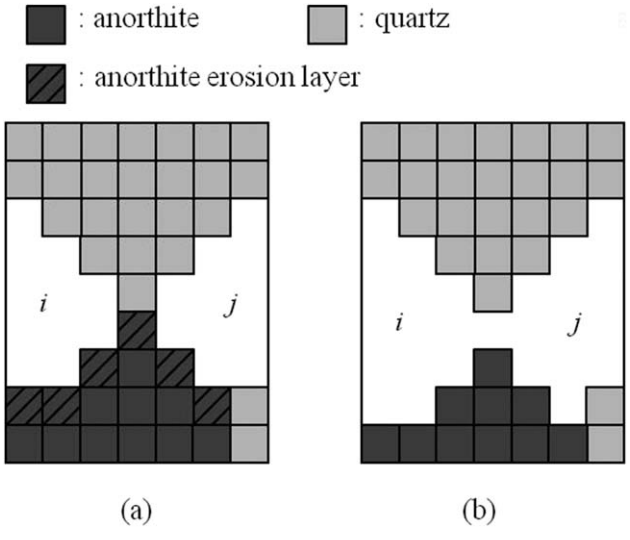

Figure 3. The 2-D illustration of a uniform, six-connected, single-voxel-layer erosion of an anorthite grain surface creating a new pore-pore connection and a new throat.

can be uniquely represented as a linear combination of the independent species; that is, a dependent species can be represented as the product of a chemical reaction with independent species written as reactants. These N_D reactions have the equilibrium equations [*Liu et al*., 2011; *Steefel and MacQuarrie*, 1996]

$$\gamma_\alpha[\alpha]=K_\alpha\prod_{\beta=1}^{N_I}\left(\gamma_\beta[\beta]\right)^{a_{\alpha\beta}},\quad \alpha=1,\ \ldots,\ N_D, \tag{3}$$

where γ_α denotes the activity coefficient for species α, K_α is the equilibrium constant for the reaction, and $a_{\alpha\beta}$ is the stoichiometric coefficient of independent species β in the reaction for species α.

[14] The total concentration, T_β, for independent species β can be written [*Liu et al*., 2011; *Steefel and MacQuarrie*, 1996]

$$T_\beta=[\beta]+\sum_{\alpha=1}^{N_D}a_{\alpha\beta}[\alpha],\quad \beta=1,\ \ldots,\ N_I. \tag{4}$$

[15] Multiplying (1) by the stoichiometric coefficient $a_{\alpha\beta}$ and summing over all species α gives

$$\frac{\partial T_\beta}{\partial t}+v\cdot\nabla T_\beta=\nabla\cdot\sum_{\lambda=1}^{N_S}\left(\sum_{\alpha=1}^{N_S}a_{\alpha\beta}D_{\alpha\lambda}\right)\nabla[\lambda]+\overline{s_\beta},\quad \beta=1,\ldots,\ N_I, \tag{5}$$

where $\overline{s_\beta}=\sum_{\alpha=1}^{N_S}a_{\alpha\beta}s_\alpha$ is the net concentration production rate for independent species β. The fast equilibrium reactions rebalance chemical species but do not change total concentrations. Therefore, the contributions to $\overline{s_\beta}$ from the fast reactions cancel each other, and only the kinetic reactions contribute. Once the total concentrations are computed from system (5), the equilibrium concentrations for all N_S species can be computed from the N_D equilibrium equations in (3) and the N_I equations in (4) (conservation of total concentrations).

[16] Note that an explicit-time numerical method can be applied directly to system (5) to solve for the total concentrations at time step $n+1$ as all individual species concentrations would be known at time step n. To use an implicit time-stepping scheme, it is advantageous to have the diffusion flux term in (5) written in total concentration form. A standard development of this gives

$$\frac{\partial T_\beta}{\partial t}+v\cdot\nabla T_\beta=\nabla\cdot\left(\sum_{\alpha=1}^{N_I}A_{\beta\alpha}\nabla T_\alpha\right)+\overline{s_\beta},\qquad \beta=1,\ldots,\ N_I, \tag{6}$$

where the matrix elements $A_{\beta\alpha}$ are given in equations (12–14) of *Liu et al*. [2011]. Note however that (6) is not reduced to a system expressed only in total concentrations; the elements $A_{\beta\alpha}$ remain (generally nonlinear) functions of the independent species concentrations. These terms are time-consuming to compute, dominate the solution time for (6), and are generally time-lagged in an implicit time scheme approach. We therefore chose an alternate approach.

[17] Recall that (5) is obtained by multiplying (1) by the stoichiometric coefficient $a_{\alpha\beta}$ and summing over all species α. In this sum, the instantaneous reaction terms cancel. Therefore, consider the following modification to system (1),

$$\frac{\partial[\alpha]}{\partial t}+v\cdot\nabla[\alpha]=\nabla\cdot\sum_{\beta=1}^{N_S}D_{\alpha\beta}\nabla[\beta]+s'_\alpha,\quad \alpha=1,\ldots,\ N_S, \tag{1'}$$

where s'_α contains *only* the slow (kinetic) reaction terms. (Note there is a subtle difference between s'_α in (1′) and $\overline{s_\beta}$ in (6). The parameter s'_α comprises the slow reaction terms for each species, and $\overline{s_\beta}$ comprises the slow reaction terms for the total concentrations of the independent species.) Equation (5) will also be obtained by multiplying (1′) by $a_{\alpha\beta}$ and summing over all species, α. We claim (and verify numerically) that solution of (1′), (3), (4) is equivalent to solution of either (5), (3), (4) or (6), (3), (4). While system (1′) is larger than (5), we expect that the extra work needed to solve the larger system (1′) under an implicit time-stepping formulation will offset the work needed to handle the solution of (6) under an implicit time-stepping formulation.

[18] With dissolution, the solid phase is no longer rigid; rather the fluid flow field will change as the volume of the anorthite phase decreases. Conservation of mass for the incompressible fluid phase is modeled by

$$\nabla\cdot v=0,\qquad v=-C\nabla P \tag{7}$$

where C is local hydraulic conductivity and P is the driving pressure (we ignore gravitational terms due to the small physical size of the domain). The flow system (7) was solved under a fixed pressure difference between inlet and outlet faces with no-flow conditions on the remaining boundaries. The dissolution changes determine changing boundary conditions for the solution of (7).

2.4. The Numerical Scheme

[19] The coupled system (1′), (3), (4), (7) was solved by a standard splitting of the system. The solution at each time step consisted of solution of (1′) for total concentrations, followed by solution of system (3), (4) in order to compute individual species concentrations, and then solution of (7) to update the flow field. The justifications for this standard splitting are (i) time scale differences between the nonlinear algebraic system (3), (4) involving instantaneous reaction rates and the differential system (1′) involving finite reaction rates, and (ii) species concentrations are sufficiently low to have negligible effect on the flow field.

[20] To compute on time scales needed to study upscaled reaction rates under network volumetric changes, an implicit time solution method is required for (1′). We applied the following scheme; to update from time step n to time step $n+1$ consider the iterative procedure (m is the iteration index)

$$\frac{[\alpha]^{m+1}-[\alpha]^n}{\Delta t}+v\cdot\nabla[\alpha]^{m+1}=\nabla\cdot\sum_{\beta=1}^{N_S}D_{\alpha\beta}\nabla[\beta]^{m+1}+s'^{\,n}_\alpha. \tag{8}$$

[21] The iterative procedure is halted when the Nernst-Planck term satisfies

$$\frac{z_\alpha z_\beta D_\alpha D_\beta [\alpha]^{m+1}}{\sum_{\lambda=1}^{N_s} z_\lambda^2 D_\lambda [\lambda]^{m+1}} - \frac{z_\alpha z_\beta D_\alpha D_\beta [\alpha]^{m}}{\sum_{\lambda=1}^{N_s} z_\lambda^2 D_\lambda [\lambda]^{m}} < \epsilon, \tag{9}$$

at which point $[\alpha]^{n+1} \equiv [\alpha]^{m+1}$. The primary purpose of the iterative scheme is to establish the correct electric potential to counter the differential charge diffusion. The equilibrium system (3), (4) was not updated during the iterative procedure in (8). If the Nernst-Planck term is ignored, the iterative procedure is not necessary and the implicit form of (8) becomes

$$\frac{[\alpha]^{n+1} - [\alpha]^n}{\Delta t} + v \cdot \nabla [\alpha]^{n+1} = \nabla \cdot \sum_{\beta=1}^{N_S} D_\beta \nabla [\beta]^{n+1} + s'_\alpha{}^n. \tag{10}$$

[22] In a pore-network model, the spatial discretization involves integration of the governing partial differential equation over the volume of a pore. Concentrations become pore averages. Suppressing the time discretization which has been discussed earlier, the spatial discretization of (1′) for species α in pore i is

$$\frac{\partial \left(V_i [\alpha]_i\right)}{\partial t} + \sum_{j|Q_{ij}>0} Q_{ij} [\alpha]_i + \sum_{j|Q_{ij}<0} Q_{ij} [\alpha]_j = \sum_j a_{ij} J_{\alpha,ij} + S_{\alpha,i} \ , \tag{11}$$

$$J_{\alpha,ij} = D_\alpha \frac{[\alpha]_j - [\alpha]_i}{l_{ij}} + z_\alpha D_\alpha [\alpha]_{ij} \frac{\sum_\beta z_\beta D_\beta \left([\beta]_j - [\beta]_i\right)/l_{ij}}{\sum_\beta z_\beta^2 D_\beta [\beta]_{ij}}, \tag{12}$$

where j indexes pores attached to i; V_i is the volume of pore i; $S_{\alpha,i}$ is the mass production rate (kinetic terms only) of species α in pore i; Q_{ij} is the volume flow rate between pores i and j (positive for outflow from i); a_{ij} and l_{ij} are the cross-sectional area and the length of the channel between pores i and j, respectively; and $[\cdot]_{ij} = ([\cdot]_i + [\cdot]_j)/2$. The volumetric flow rate is related to the channel velocity v_{ij} by $Q_{ij} = a_{ij} v_{ij}$. The spatial discretizations of (5), (8), and (10) are similar.

[23] Integrating over the volume of a pore element, the spatial discretization of (7) is

$$\sum_j Q_{ij} = \sum_j C_{ij} (P_i - P_j) = -\frac{S_{A,i}}{\rho_A}, \tag{13}$$

where P_i and P_j are respective pressures in, and C_{ij} is the conductance between, pores i and j; ρ_A (2.73 g cm^{-3}) is the anorthite density; and $S_{A,i}$ is the anorthite mass dissolution rate in pore i. The right-hand side, $-S_{A,i}/\rho_A$, is the volume expansion rate of V_i resulting from anorthite dissolution. The form of $S_{A,i}$ is given in section 2.7. Channel conductance C_{ij} was computed using the model of *Patzek* [2001], based upon cross-sectional shape factor values assuming either triangular, rectangular, or circular cross-sectional shape for a conducting unit (with exact choice based upon shape factor magnitude). Further details on our implementation of the Patzek model can be found in *Sholokova et al*. [2009], where the model is referred to as network flow - series resistance conductance (NF-SRG).

[24] The time-step update of (13) is

$$\sum_j C_{ij}^{\overline{n+1}} \left(P_i^{n+1} - P_j^{n+1}\right) = \frac{-S_{A,i}^{\overline{n+1}}}{\rho_A}. \tag{14}$$

[25] The notation $\overline{n+1}$ indicates that the corresponding variables are time t^{n+1} updates obtained from the geometrical changes produced from the solution of (8) (or (10)) and are, for purposes of solution of the pore pressures in (14), known values. The pore pressures P_i, and hence the volumetric flow rates Q_{ij}, were updated each time step by applying conjugate gradient iteration with symmetric successive over-relaxation (SSOR) preconditioning [*Trefethen and Bau*, 1997] to the linear system (14). Pore pressure values from the previous time step were used to initialize the conjugate gradient iterations.

[26] To test the ability of (1′) to return accurate total concentrations, we compared solution of (5), (3), (4) against (1′), (3), (4), with and without the inclusion of the Nernst-Planck term in the diffusion flux, using the explicit time-stepping scheme,

$$\frac{[\alpha]^{n+1} - [\alpha]^n}{\Delta t} + v \cdot \nabla [\alpha]^n = \nabla \cdot \sum_{\beta=1}^{N_S} D_{\alpha\beta} \nabla [\beta]^n + s'_\alpha{}^n, \tag{15}$$

with appropriately small time steps. These test computations were done in the pore network *assuming no* geometric change with reaction. (Thus, the flow field computation (13) had to be performed only once.) Comparison of the results for 3000 s of flow (5.5×10^5 time steps) is shown in Figure 4a. The comparison is shown in terms of the relative error

$$\varepsilon_{1',5,\alpha} \equiv \left| \frac{R_{N,\alpha}(1') - R_{N,\alpha}(5)}{R_{N,\alpha}(5)} \right|, \quad \alpha = A, K. \tag{16}$$

[27] In (16) $R_{N,\alpha}$(k) denotes the upscaled reaction rate for mineral α computed by simulation using equation (k). For the computations without the Nernst-Plank term, the relative error is bounded below 2×10^{-7}. For the computations including the Nernst-Plank term, the relative error shows growth at larger times. Since under conditions of no geometric change, the reaction rates are effectively in steady state long before 3000 s [see *Kim and Lindquist*, 2011, Figure 1], the continued growth of the relative error when the Nernst-Plank term is included may disappear under a reduction in the time-step size in the explicit method.

[28] Comparison of the results for the solution of (1′), (3), (4) on the test network using the implicit time-stepping schemes (8) and (10) (with and without the Nernst-Planck term) with the results of the solution of (1′), (3), (4) obtained using explicit time-stepping (15) is given in Figure 4b. Here the relative errors are computed as $\varepsilon_{10,15,\alpha}$ (for the computation without the Nernst-Plank term) and as $\varepsilon_{8,15,\alpha}$ (for the computation with the Nernst-Plank term). The definitions of $\varepsilon_{10,15,\alpha}$ and $\varepsilon_{8,15,\alpha}$ follow directly from (16). Here the relative errors remain bounded by 2.5×10^{-4}. The results in Figure 4 give confidence in the use of formulation (1′) to deliver total concentrations consistent with (5).

2.5. The Reactions

[29] The reactions studied, involving kaolinite and anorthite with acidic brine, comprise a system of 11 reactions: 9 of which are aqueous and are modeled as instantaneous and 2 of which are surface reactions involving the solid species and are modeled kinetically [*Li et al*., 2006]. The surface reactions are

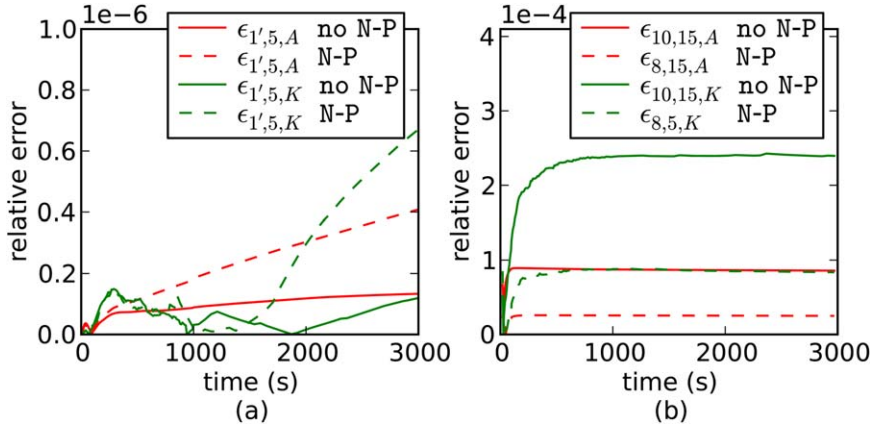

Figure 4. (a) Comparison of solution to system (1′), (3), (4) with the solution to (5), (3), (4), both with and without the Nernst-Planck (N-P) term included, using the explicit scheme (15). (b) Comparison of solutions to system (1′), (3), (4) using the implicit methods (10) (no N-P term) or (8) (with N-P term) with solutions obtained using the explicit method (15). The relative errors $\varepsilon_{j,k,\alpha}$ are defined by (16) and discussed in the text. These test calculations were run with no geometrical changes in the medium resulting from the surface reactions and hence with a time-invariant flow field having average Darcy velocity of 5.8×10^{-3} cm s^{-1}.

$$\text{anorthite}: \quad CaAl_2Si_2O_8(s) + 8H^+ \leftrightarrow Ca^{2+} + 2Al^{3+} + 2H_4SiO_4, \tag{17}$$

$$\text{kaolinite}: \quad Al_2Si_2O_5(OH)_4(s) + 6H^+ \leftrightarrow 2Al^{3+} + 2H_4SiO_4 + H_2O. \tag{18}$$

[30] The laboratory-determined rate laws (mol m^{-2} s^{-1}) for (17) and (18) are given by

$$r_\alpha = r_{\mathrm{pH},\alpha}\, f_{\Omega,\alpha}, \qquad \alpha = \mathrm{A\ (anorthite)\ or\ K\ (kaolinite)}, \tag{19}$$

where $r_{\mathrm{pH},\alpha}$ reflects the kinetics of the pH and $f_{\Omega,\alpha}$ captures dependency on the saturation state, Ω_α. The r_{pH} terms for the reactions are

$$r_{\mathrm{pH},A} = k_{H^+,A}\{H^+\}^{1.5} + k_{H_2O,A} + k_{OH^-,A}\{OH^-\}^{0.33}, \tag{20}$$

$$r_{\mathrm{pH},K} = k_{H^+,K}\{H^+\}^{0.4} + k_{OH^-,K}\{OH^-\}^{0.3}. \tag{21}$$

[31] The saturation states are

$$\Omega_A \equiv \frac{\{Ca^{2+}\}\{Al^{3+}\}^2\{H_4SiO_4\}^2}{\{H^+\}^8 K_{eq,A}}, \tag{22}$$

$$\Omega_K \equiv \frac{\{Al^{3+}\}^2\{H_4SiO_4\}^2}{\{H^+\}^6 K_{eq,K}}, \tag{23}$$

where $\{\beta\} = \gamma_\beta[\beta]$ represents the chemical activity of species β. Values of the rate constants and equilibrium constants in (20)–(23) were based on experimental studies [*Amrhein and Suarez*, 1988; *Brady and Walther*, 1989; *Carroll and Walther*, 1990; *Ganor et al*., 1995; *Helgeson et al*., 1984; *Nagy et al*., 1991; *Oelkers and Schott*, 1995], adjusted to the simulation temperature using the Arrhenius equation, and were summarized in Table 1 of *Kim et al*. [2011].

[32] The forms for f_Ω in dissolution and precipitation modes are

$$\begin{array}{ll} \text{dissolution} & \text{precipitation} \\ f_{\Omega,A} = 1 - \Omega_A, & f_{\Omega,A} = 1 - \Omega_A, \\ f_{\Omega,K} = 1 - \Omega_K^{0.9}, & f_{\Omega,K} = \Omega_K^{-1.9} - 1\,. \end{array} \tag{24}$$

[33] The forms for $f_{\Omega,A}$ in (24) and the form of $f_{\Omega,K}$ in (25) in the dissolution mode for kaolinite are in good agreement with existing data. However, the precipitation regime of kaolinite is less well characterized at large saturation state values. In *Kim and Lindquist* [2011] we considered three forms for $f_{\Omega,K}$ in the precipitation range. In this paper we focus on the form suggested by *Nagy and Lasaga* [1993] in which their data were fit to a relation derived from transition state theory. This form produces a bounded reaction rate at large saturation state values.

[34] The rates (18) were used for the surface reactions occurring locally within a single pore. This assumes that mass transfer is not limiting, and the aqueous concentrations are spatially uniform within a pore. A check on this assumption using a Damköhler number calculation has been previously published [*Li et al*., 2006]. (However, see commentary on this in section 4.)

[35] The aqueous system of nine reactions is shown in Table 1. Thus, the reactive system (kinetic plus instantaneous) involved 17 species, 6 of which (H_2O; H^+; $H_2CO_3^*$, representing carbon-bearing species; H_4SiO_4, representing silicon-bearing species; Al^{3+}; and Ca^{2+}) are independent. The reactions in Table 1 are written with dependent species as product. Equilibrium constants were taken from *Morel and Hering* [1993], were adjusted for temperature using SUPCRT92 [*Johnson et al*., 1992], and are also given in Table 1. Activity coefficients for all species in the reaction model were estimated by the Davis equation [*Benjamin*, 2002] and assumed constant.

[36] Solution of the coupled system (3), (4) requires a nonlinear method such as Newton-Raphson. The system in Table 1 has a simplifying feature; H^+ is the only independent species reactively coupled to each of the dependent

Table 1. Instantaneous Reactions[a]

Reaction	$\log_{10} K_{eq}$	Reaction	$\log_{10} K_{eq}$
$H_2O - H^+ \leftrightarrow OH^-$	−13.2	$Al^{3+} + H_2O - H^+ \leftrightarrow Al(OH)^{2+}$	−4.44
$H_2CO_3^* - H^+ \leftrightarrow HCO_3^-$	−6.15	$Al^{3+} + 2H_2O - 2H^+ \leftrightarrow Al(OH)_2^+$	−8.5
$H_2CO_3^* - 2H^+ \leftrightarrow CO_3^{2-}$	−16.15	$Al^{3+} + 3H_2O - 3H^+ \leftrightarrow Al(OH)_3$	−12.3
$H_4SiO_4 - H^+ \leftrightarrow H_3SiO_4^-$	−9.2	$Al^{3+} + 4H_2O - 4H^+ \leftrightarrow Al(OH)_4^-$	−19.6
$H_4SiO_4 - 2H^+ \leftrightarrow H_2SiO_4^{2-}$	−21.6		

[a]The reactions are written with independent species as reactants and dependent species as products. The equilibrium constants have been adjusted for this form.

species. As a consequence, ignoring the independent species Ca^{2+} which decouples completely, the activity of each of the other four independent species can be expressed as a function of $\{H^+\}$ and the five total concentrations [*Kim*, 2008]. Thus, the solution of (3), (4) reduces to a scalar root-finding problem to determine a value for $\{H^+\}$, which corresponds to the value for the total concentration of H^+ obtained from (1′). This results in a faster, more robust solution method.

2.6. Network Simulations

[37] Each network simulation was performed on the pore network obtained from sample 3W4 under a constant pressure drop between the inlet and outlet faces. Four different pressure drops were simulated; the pressure drops produced initial, bulk-averaged Darcy velocities of 5.8×10^{-3}, 1×10^{-3}, 1×10^{-4} and 1×10^{-5} cm s^{-1}. (As dissolution proceeded, porosity increased, and the bulk-averaged Darcy velocity grew with time in each simulation. We use the initial value of the Darcy velocity to label each simulation.) This represents an extremely wide range of flow conditions, from those that might be experienced near a well bore, to those characteristic of far-field conditions. Each simulation began with the pore network saturated with saline water (50°C, pH 6.6, dissolved solid concentrations $[Na^+] = [Cl^-] = 0.45$ *M*, $[Ca^{2+}] = 7.9 \times 10^{-6}$ *M*) in reactive equilibrium with the aqueous system of reactions in Table 1. Acidic saline solution (50°C, pH 3.01, $[Na^+] = [Cl^-] = 0.45$ *M*, $[Ca^{2+}] = 7.9 \times 10^{-6}$ *M*) with dissolved CO_2 (in the form of $H_2CO_3^*$) was injected at the inlet. The concentration of $H_2CO_3^*$ was determined by the solubility of CO_2 (1.01 *M*) at 100 bar and 50°C. The remaining species in the injected solution were determined from Table 1 and the condition that their concentrations are in equilibrium with that of $H_2CO_3^*$.

2.7. Upscaled Rates, R_N, From the Network Model

[38] The mass production rates $S_{K,i} = r_{K,i} A_{K,i}$ (mol s^{-1}) of kaolinite and $S_{A,i} = r_{A,i} A_{A,i}$ (mol s^{-1}) of anorthite were computed for each pore *i*. Upscaled reaction rates, R_N (mol m^{-2} s^{-1}), for the entire core (pore-network) can be defined by

$$R_{N,\alpha} = \frac{\sum_i S_{\alpha,i}}{\sum_i A_{\alpha,i}}, \qquad \alpha = K, A. \tag{26}$$

[39] The network upscaled rates, R_N, incorporate mass balance, account for the network, mineral, and flow heterogeneities captured by the network reactive flow model as well as the microscale rate laws.

2.8. Upscaled Rates, R_C, From a Continuum Model

[40] The network results were compared against a continuum formulation which uses spatially averaged values to represent system properties and uses uniform concentrations in the laboratory-based rate laws to compute continuum-scale reaction rates. The continuum model was constrained to the same hydrodynamic and reactive properties, reactive system, and initial and boundary conditions as the network model. The mass balance equation in the continuum formulation is obtained by integrating (1′) over the entire pore network,

$$\frac{dV_T[\alpha]_C}{dt} + Q_T[\alpha]_C - Q_T[\alpha]_{\text{in}} = S_{\alpha_C}, \tag{27}$$

where $[\alpha]_C$ is the continuum concentration and $[\alpha]_{\text{in}}$ is the inflow concentration for species α; V_T and Q_T are the total pore volume and total flow rate, respectively. In the continuum formulation, the entire volume is characterized by a single concentration, and the diffusion flux vanishes. The mass production rate terms, S_{α_C}, are given in *Kim* [2008]. For example, $S_{H^+C} = -8R_{C,A}A_{A,T} - 6R_{C,K}A_{K,T}$, where $A_{A,T}$ and $A_{K,T}$ are the total reactive surface areas for anorthite and kaolinite in the network model, and $R_{C,A}$ and $R_{C,K}$ are evaluated from the laboratory-based rate laws (19) using continuum concentrations and activities (e.g., $R_{C,K} = \left(k_{H^+,K}\{H^+\}_C^{0.4} + k_{OH^-,K}\{OH^-\}_C^{0.3}\right) f_{\Omega,C}$) where $f_{\Omega,C}$ is given by (25) computed using continuum activity values). In the continuum formulation, the equilibrium system (3), (4) is solved using continuum concentrations and activities.

3. Results

[41] The total mass of flow-accessible anorthite in our network model was 2.45×10^{-6} mol. Complete dissolution of this mass of anorthite resulted in a 2.2% (11.9% → 14.1%) increase in porosity in the network. As a result of this porosity change with time, the permeability of the network increased from 108 to 151 mD (hence, the average Darcy velocity through the network increased with time). Under anorthite dissolution, the number of pores remained unchanged at 5,329, but the number of pore-pore connections increased by 11% (8762 → 9702). Initially, 1.3% of the total pore surface area was anorthite grain, 58.8% was kaolinite, and 39.9% was quartz. Figure 5 plots the total pore-exposed anorthite surface area, $A_{A,T}$, as a function of total dissolved anorthite mass, M_A. The total anorthite surface area increased initially, before falling to zero as all accessible anorthite dissolved. Anorthite dissolution exposed more kaolinite surface area, which increased from 238 to 243 cm^2.

[42] Figure 6 shows the results for the computed upscaled reaction rates $R_{N,A}$ and $R_{N,K}$ for the four computations done

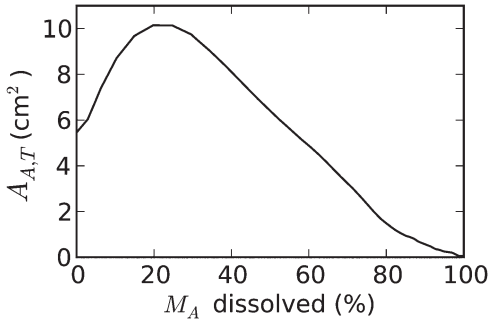

Figure 5. Total pore-exposed anorthite surface area as a function of total mass of anorthite dissolved.

at different initial average flow velocities. These computations are done without the Nernst-Planck term. As the time scales for total anorthite dissolution vary with flow rate, the reaction rates are presented as a function of anorthite mass dissolved. For each initial velocity, the upscaled rate behavior with time displayed different behaviors. The reaction rate behavior can be broken into three stages: an initial transient, when the acid rich inflow first invades; the long-term reaction rate after most anorthite has been consumed; and intermediate-time behavior accompanying the geometric changes from anorthite dissolution.

3.1. Initial Transient Behavior

[43] The previous studies [*Kim and Lindquist*, 2011; *Kim et al*., 2011], done without modeling geometric change, showed the following behavior. For the anorthite reaction, which is far from equilibrium, the upscaled reaction rate rose relatively rapidly to a steady-state dissolution value. For the kaolinite reaction which is closer to equilibrium, the upscaled rate initially rose, generally to a positive dissolution value, and then fell to a steady-state value. For kaolinite, depending on bulk flow rate, this was generally a steady-state precipitation value. The early time behavior of the present computations (inset plots in Figure 6) revealed virtually identical results to those seen in the previous studies. For anorthite, the initial transient results in a rapidly increasing $R_{N,A}$ to a "steady" dissolution value; the faster the velocity of injection, the higher the dissolution rate. For kaolinite there is a brief rise in $R_{N,K}$ (dissolution) followed by a drop to a "steady" value that is precipitative, except at the highest flow velocity. Thus, the early time behavior, $0 < M_A$ dissolved $< 0.3\%$, which involves little geometric change, captures essentially the entire behavior observed in earlier published results [*Kim and Lindquist*, 2011; *Kim et al*., 2011] where geometric changes were excluded. The remaining (and the majority of the) behavior shown in Figure 6 chronicles the effects enabled by geometrical change.

3.2. Long-Term (Stage 3) Behavior

[44] Once all anorthite is dissolved, $R_{N,A}$ must vanish. After all anorthite has been consumed, the kaolinite reaction rate must be anorthite-independent. With all anorthite dissolved, the kaolinite reaction becomes Al^{3+} starved, and as we did not model kaolinite geometric changes, $R_{N,K}$ must approach a steady-state positive value. The value of this large-time dissolution rate will decrease with decreasing flow rate (as indicated in our previous work). We ran the simulation up to 90% anorthite mass dissolution at the slowest flow rate (1.0×10^{-5} cm s^{-1}) and only up to 70% mass dissolution at the highest flow rate (5.8×10^{-3} cm s^{-1}). (The discussion later on Figure 7 addresses runtime considerations in greater detail.) The plots in Figure 6 are consistent with $R_{N,A} \to 0$ at the largest times simulated; however (especially at the slower flow rates where we were able to compute to higher anorthite mass dissolution), they are also consistent with $R_{N,A}$ remaining finite (bounded away from 0) as long as accessible anorthite surface area remains. This second conclusion may be more likely given that the definition of $R_{N,A}$ (26) uses a denominator of anorthite surface area rather than total grain surface area. In Figure 6 we see $R_{N,K}$ rising toward positive (dissolution) values, beginning this rise by values of as low as 40%

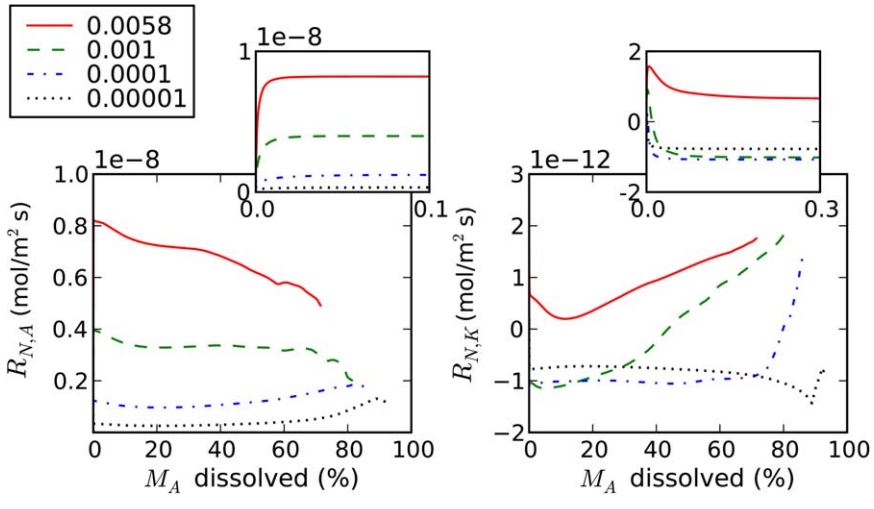

Figure 6. Anorthite and kaolinite upscaled reaction rates as a function of total mass of anorthite dissolved for the four initial Darcy flow rates. The computations were done without the Nernst-Planck diffusion term. The insets show the detail at early time. This early time behavior captures the totality of behavior observed in earlier published results when no geometric changes are included.

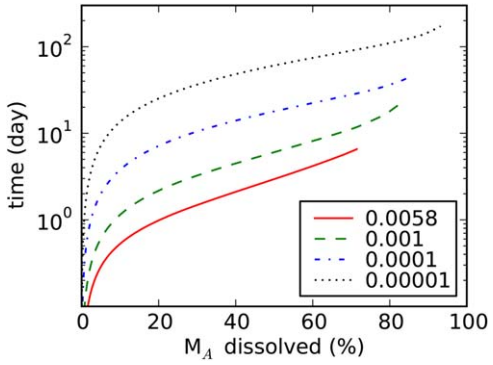

Figure 7. Simulated time versus dissolved anorthite mass for the four different initial Darcy velocities.

anorthite mass dissolution for the calculation with the initial injection rate of 1×10^{-3} cm s^{-1}, by 80% for the calculation with initial rate of 1×10^{-4} cm s^{-1}, and by 90% for the computation at the slowest injection rate.

3.3. Intermediate-Time (Stage 2) Behavior

[45] Geometric change accompanying anorthite dissolution is necessary for the observed intermediate-time behavior to occur but is not sufficient to describe all that does occur. This intermediate-time behavior connecting early transient (no geometric change) to long-term behavior (when most geometric change is complete) is affected by the geometric changes as well as by the factors, essentially pH and saturation state, governing the microscopic rate laws. The anorthite dissolution rate is dominated by $r_{\mathrm{pH},A}$ ($f_{\Omega,A} \sim 1$ everywhere in the network) [*Kim and Lindquist*, 2011; *Kim et al*., 2011] which, in turn, is dominated by [H^+]. H^+ concentration was maintained via the acid injection and was consumed by anorthite dissolution. The initial geometric changes resulting from dissolution increased the anorthite surface area in the network (Figure 5). This surface area reached a maximum value after approximately 20% anorthite mass dissolution. Over this period, dissolution-consumption of H^+ combined with the increase in anorthite surface area resulted in a drop in $R_{N,A}$ in each simulation.

[46] Beyond 20% anorthite mass dissolution, the anorthite surface area decreased and the behavior of $R_{N,A}$ changed with the simulation, i.e., with the flow rate. At the highest flow rate modeled (5.8×10^{-3} cm s^{-1}), $R_{N,A}$ continued to steadily decrease. We postulate this is due to the heterogeneities in $A_{A,i}$ in the network at this high injection rate. Values of $A_{A,i}$ in (26) are relatively small in fast dissolution pores and large in slow dissolution pores. The net effect is uneven [H^+] distribution, a wide variation of local anorthite dissolution rates, and a value for $R_{N,A}$ that continued to decrease (from 7×10^{-9} mol m^{-2} s^{-1} at 20% anorthite mass dissolution to 5×10^{-9} mol m^{-2} s^{-1} at 70% anorthite mass dissolution). At the slowest injection rate modeled (1×10^{-5} cm s^{-1}), the network developed a more uniform distribution in [H^+], and heterogeneities in $A_{A,i}$ became weaker. As a result, $R_{N,A}$ then increased (from 2.5×10^{-10} mol m^{-2} s^{-1} at 20% anorthite mass dissolution to 1×10^{-9} mol m^{-2} s^{-1} at 90% anorthite mass dissolution) as the decreasing anorthite surface area decreased consumption of H^+ while increasing medium permeability enabled faster intake of acidic fluid from the inlet boundary. In the calculation with initial injection rate of 1×10^{-3} cm s^{-1}, $R_{N,A}$ was relatively constant over the period from 20% to 70% total dissolved anorthite mass, implying that these opposing factors were relatively balanced.

[47] In understanding the intermediate-time behavior of $R_{N,K}$ note that while the two mineral reactions are coupled, the anorthite kinetics are faster than kaolinite. At the highest injection rate (5.8×10^{-3} cm s^{-1}), as the anorthite reactive surface area increased to a maximum value, increased production of Al^{3+} and H_4SiO_4 by anorthite dissolution reduced $f_{\Omega,K}$ further and decreased $R_{N,K}$ to a minimum rate (attained then the anorthite reactive surface area was maximized). As anorthite dissolution then slowed, decreasing [Al^{3+}] and [H_4SiO_4] and enabling an increase in [H^+], $R_{N,K}$ then increased toward its long-term value.

[48] At the slowest injection rate (1×10^{-5} cm s^{-1}), following the initial transient $R_{N,K}$ was already negative with kaolinite precipitating in all pores and $f_{\Omega,K} = -1$ in most pores, remaining so until 90% of anorthite was dissolved. Over this period, $R_{N,K}$ depended only on $r_{\mathrm{pH},K}$ (i.e., on pH) which was affected by the H^+-consuming anorthite dissolution and by the gradually increasing acidic injection due to increased permeability accompanying pore volume increase. The average pH increased ($|R_{N,K}|$ decreased) until the anorthite surface area maximized, subsequently the pH decreased ($|R_{N,K}|$ increased) reaching an extremum around 90% of anorthite dissolution. As the remaining 10% of the available anorthite dissolved, $f_{\Omega,K}$ increased dramatically and $R_{N,K}$ started its rapid increase to a long-term steady-state value.

[49] Figure 7 plots simulation time versus dissolved anorthite mass for the different computations. The plots illustrate the difficulty in computing to 100% anorthite mass loss (i.e., to the long-term regime). Over most of the mid-range (20%–80%) of anorthite mass loss, simulation time grows exponentially, with growth rates that increase with flow velocity. There is an indication that in the final 20% of anorthite mass loss, this exponential growth rate is exceeded. Unless the numerical method can accommodate a Δt that roughly doubles in size each time step (i.e., $\Delta t_{n+1} \cong 2\Delta t_n$) as the anorthite is used up, computational time becomes an issue. The simulations shown here were halted after 0.75 weeks (slowest injection rate) to 3 weeks (fastest injection rate) of "wall-clock" time on a 4-core processor.

[50] Table 2 lists the time-step intervals used for the explicit and implicit schemes for each simulation performed at a different initial bulk flow rate. The number of iterations of (8) required to advance from time step n to $n+1$ obviously varied with the tolerance value ϵ, with time, t, as well as with flow velocity. At the highest flow velocity, as many as 22 iterations were required to advance a time step.

Table 2. Time-Step Sizes

Initial Flow Rate (10^{-5} cm s^{-1})	Δt (s)	
	Explicit Scheme	Implicit Scheme
580	0.0055	0.13
100	0.018	0.7
10	0.035	2.0
1	0.040	5.0

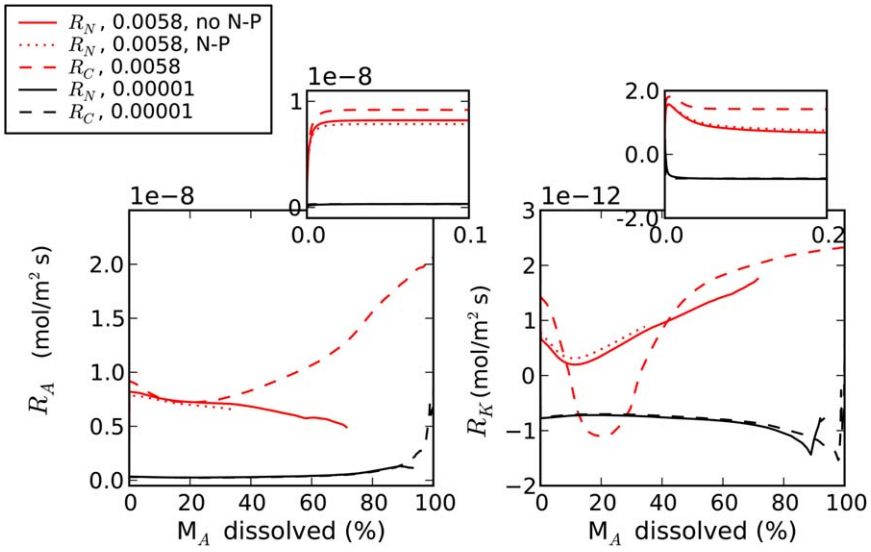

Figure 8. Comparison of upscaled flow rate computations for (solid line) the network model without Nernst-Planck term, (dotted line) the network model with Nernst-Planck term, and (dashed line) the continuum model at the two extremes of the bulk flow the Darcy velocity range investigated. The insets show the detail at early time.

[51] For the computations performed without the Nernst-Planck term at the fastest and slowest flow velocities Figure 8 compares the continuum computation upscaled values $R_{C,A}$ and $R_{C,K}$ with those from the network model, $R_{N,A}$ and $R_{N,K}$. In our previous work (without geometric changes) we observed that R_C and R_N tended to agree under one or more of the following conditions: (i) the pH was relatively uniform throughout the medium; (ii) the reaction was far from equilibrium (reducing the impact of any heterogeneity in saturation states); and (iii) the flow rate was slow (reducing the impact on advection driven variation in concentrations) [*Kim and Lindquist*, 2011; *Kim et al*., 2011]. In agreement with these observations, we note the early time agreement (Figure 8 inset plots) between R_C and R_N except for the kaolinite reaction at the fastest injection rate. Once geometric changes occur, agreement between R_C and R_N is still fairly good at the slowest flow rate, until 80%–90% of the anorthite mass is dissolved. Afterward, the predictions of the two methods diverge rapidly. At the fastest velocity, the continuum model has poor agreement with the network model: (i) over the entire time for kaolinite (reaction close to equilibrium) and (ii) for anorthite once 40% of the anorthite has dissolved.

[52] The computations in Figures 6–8 discussed earlier were run without the Nernst-Planck term. We now consider the effect of the importance of including the electrical neutrality correction. We therefore also plot in Figure 8 the upscaled reaction rates obtained using the Nernst-Planck term for computation at the fastest flow rate. These computations with the Nernst-Planck term were only run to 40% anorthite dissolution due to the extensive CPU time required. We measured the relative error between the calculations with and without the N-P term using a pore-by-pore L_1 norm,

$$\text{relative error} = \frac{\sum_i |r^{NP}_{i,\alpha} A^{NP}_{i,\alpha} - r_{i,\alpha} A_{i,\alpha}|}{\sum_i |r^{NP}_{i,\alpha} A^{NP}_{i,\alpha}|}, \tag{28}$$

where the sum, i, is over pores. The average relative error for the anorthite reaction is 8.8%; that for the kaolinite reaction is 7.2%. Computations with the Nernst-Planck term at the other flow rates were also performed. The agreement (not shown) between simulations with and without the Nernst-Planck term improved as the flow rate decreased.

4. Discussion

[53] When geometrical changes are not included, the core-scale reaction rates reached steady state in a relatively short period of time (inset plots Figure 6) [*Kim*, 2008; *Kim and Lindquist*, 2011]. We have previously suggested that such steady-state, core-scale reaction rates could be used as input into larger-scale simulations. Our current results however indicate that the geometrical changes accompanying reactions result in continuously time-dependent upscaled rates that would need to be characterized (e.g., as a function of remaining anorthite mass) before being used in larger-scale computations. For the reactions studied here, the upscaled rates are ultimately constrained to change from what they are initially to what they must be when all accessible anorthite is dissolved. The geometrical changes induced by dissolution contribute to the "functional form" between these endpoints. However, the functional form is also dependent on the microscopic rate law (i.e., on saturation state and pH); in addition, it exhibits a strong dependence on bulk flow rate, complicating the attempt to determine a general form. Our results indicate that for reactions far from equilibrium, such as the anorthite reaction modeled here, this functional form may vary less dramatically; however, reactions close to equilibrium conditions, such as the kaolinite reaction modeled here, require much more accurate characterization in order to correctly capture the upscaled reaction rate transition from precipitation to dissolution regimes with time.

[54] At high flow rates, there was significant disagreement between the rate computations of the continuum and

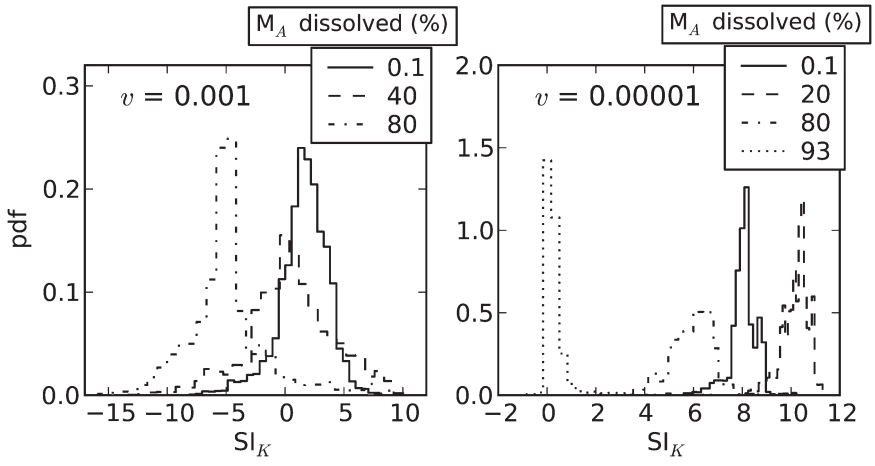

Figure 9. Time snapshots of the evolution of the distribution of saturation index $\mathrm{SI}_{\Omega,K} \equiv \log(\Omega_K)$ for the computations at initial Darcy velocities of 10^{-3} and 10^{-5} cm s^{-1}.

network formulations. The agreement improved at slow flow rates where variation in species concentrations in the network model is less severe. The reasons for the disagreement differ for the two reactions. For kaolinite, the significant upscaling issue is to capture the net effect of $f_{\Omega,K}$, i.e., the net effect of Ω_K, especially near equilibrium. Figure 9 illustrates the problem. For the computation with the initial flow rate of 10^{-3} cm s^{-1}, the distribution of $\mathrm{SI}_{\Omega,k} \equiv \log(\Omega_k)$ contained significant numbers of pores with positive (precipitation) and negative (dissolution) values. The resulting upscaled rate $R_{N,K}$ is a network average over these pores. The continuum rate, $R_{C,K}$, results from a single value of Ω_k, which if not correctly computed, stands a significant chance of incorrectly computing not just the magnitude, but the sign of the reaction rate. For the computation at the significantly slower rate of 10^{-5} cm s^{-1}, every pore in the network was in precipitation mode $(\mathrm{SI}_{\Omega,k} > 0)$ until most of the anorthite dissolved (i.e., the reaction was far from equilibrium through most of the anorthite dissolution regime). In this case, approximating the Ω_K distribution by a single value is not so critical, and the agreement between $R_{N,K}$ and $R_{C,K}$ improves.

[55] For anorthite, the reaction was always far from equilibrium. Here the significant upscaling issue is to capture the variation in the reactive surface area for this mineral (i.e., the variation in geometric changes) because of its influence on local pH. The continuum computation assumes a uniform rate of reactive surface area change throughout the medium. As a result, $R_{C,A}$ tracks the behavior of the average pH. The network computation captured the spatial variation in anorthite reactive surface area change. At slow flow rates, the average rate of reactive surface area change had small variation throughout the network, and $R_{N,A}$ does track the behavior of the average pH. However at high flow rates, reactive surface area was rapidly consumed in rapidly dissolving pores and less rapidly consumed in slowly dissolving pores, and the behavior of $R_{N,A}$ deviated significantly from that predicted by average pH.

[56] Inclusion of the Nernst-Planck term produced a correction in the prediction of $R_{N,A}$ and $R_{N,K}$ of 8%–9% at the highest flow rate. The correction decreased at slower flow rates.

[57] Pore-network models, such as that developed here, use pores as the fundamental unit of discretization. Each pore, and each pore-pore connection, is represented by single, average values for physical/chemical properties (e.g., volume, surface area, conductivity, flow rate, and species concentration). This poses the question as to how accurately computations based upon pore average values will capture reactive effects. In our computations, we employed the rates (18), which are determined from well-mixed batch reaction experiments, for reactions occurring locally within a single pore. This was predicated on an assumption that at this scale, mass transfer is not limiting and the aqueous concentrations are spatially uniform within a pore. While a check of this assumption using an estimate of a Damköhler number for H^+ has been previously published [*Li et al*., 2006], our analysis in the Appendix of *Kim et al*. [2011] shows that for the reactive system studied here there are 15 Peclet numbers (one for each aqueous species) and 3 Damköhler numbers (associated with H^+, OH^-, and H_2O). These Damköhler numbers are linearly coupled by values of their activity coefficients. Thus, we question the assumption that individual species' Damköhler numbers (whose definitions are based upon scalar advection-diffusion-reaction equations employing constant coefficients and first-order chemical kinetics) are appropriate dimensionless quantities to indicate reaction regimes in complex reactions involving nonlinear reaction rates and coupled systems. The question of the accuracy of pore-network models in computing reactive flow will require continued investigation.

[58] **Acknowledgments.** This work was supported by the U.S. Department of Energy under contracts DE-FG02–92ER14261 and DE-FG02–09ER64747.

References

Amrhein, C., and D. L. Suarez (1988), The use of a surface complexation model to describe the kinetics of ligand-promoted dissolution of anorthite, *Geochim. Cosmochim. Acta*, *52*(12), 2785–2793.

Benjamin, M. M. (2002), *Water Chemistry*, 668 pp., McGraw-Hill, New York.

Brady, P. V., and J. V. Walther (1989), Controls on silicate dissolution rate in neutral and basic pH solutions at 25 °C, *Geochim. Cosmochim. Acta*, *53*(11), 2823–2830.

Carroll, S. A., and J. V. Walther (1990), Kaoliniate dissolution at 25 °C, 60 °C, and 80 °C, *Am. J. Sci.*, *290*(7), 797–810.

Ganor, J., J. L. Mogollon, and A. C. Lasaga (1995), The effect of pH on kaolinite dissolution rates and on activation-energy, *Geochim. Cosmochim. Acta*, *59*(6), 1037–1052.

Helgeson, H. C., W. M. Murphy, and P. Aagaard (1984), Thermodynamics and kinetic constraints on reaction-rates among minerals and aqueous-solutions: 2. Rate constants, effective surface-area, and the hydrolysis of feldspar, *Geochim. Cosmochim. Acta*, *48*(12), 2405–2432.

Johnson, J. W., E. H. Oelkers, and H. C. Helgeson (1992), SUPCRT92: A software package for calculating the standard molal thermodynamic properties of minerals, gases, aqueous species, and reactions from 1 to 5000 bar and 0 to 1000 °C, *Comput. Geosci.*, *18*(7), 899–947.

Kim, D. (2008), *Scale-Up of Reactive Flow Through Network Flow Modeling*, 88 pp., Stony Brook Univ., Stony Brook, N. Y.

Kim, D., and W. B. Lindquist (2011), Dependence of pore-to-core upscaled reaction rate on flow rate in porous media, *Transp. Porous Media*, *89*(3), 459–473.

Kim, D., C. A. Peters, and W. B. Lindquist (2011), Up-scaling geochemical reaction rates accompanying acidic CO2-saturated brine flow in sandstone aquifers, *Water Resour. Res.*, *47*, W01505, doi:10.1029/2010WR009472.

Lee, T. C., R. L. Kashyap, and C. N. Chu (1994), Building skeleton models via 3-D medial surface/axis thinning algorithms, *CVGIP: Graph. Models Image Proc.*, *56*, 462–478.

Li, L., C. A. Peters, and M. A. Celia (2006), Upscaling geochemical reaction rates using pore-scale network modeling, *Adv. Water Resour.*, *29*(9), 1357–1370.

Li, L., C. A. Peters, and M. A. Celia (2007), Effects of mineral spatial distribution on reaction rates in porous media, *Water Resour. Res.*, *43*, W01419, doi:10.1029/2005WR004848.

Lindquist, W. B., A. Venkatarangan, J. Dunsmuir, and T.-f. Wong (2000), Pore and throat size distributions measured from sychrotron X-ray tomographic images of Fontainebleau sandstones, *J. Geophys. Res.*, *105*(B9), 21,508–21,528, doi:10.1029/2000JB900208.

Liu, C., J. Shang, and J. M. Zachara (2011), Multispecies diffusion models: A study of uranyl species diffusion, *Water Resour. Res.*, *47*, W12514, doi:10.1029/2011WR010575.

Lorensen, W. E., and H. E. Cline (1987), Marching cubes: A high resolution 3-D surface construction, *ACM Comput. Graph.*, *21*, 163–169.

Morel, F., and J. G. Hering (1993), *Principles and Applications of Aquatic Chemistry*, 596 pp., John Wiley, New York.

Nagy, K. L., and A. C. Lasaga (1993), Simultaneous precipitation kinetics of kaolinite and gibbsite at 80 °C and pH 3, *Geochim. Cosmochim. Acta*, *57*(17), 4329–4335.

Nagy, K. L., A. E. Blum, and A. C. Lasaga (1991), Dissolution and precipitation of kaolinite at 80 °C and pH 3—The dependence on solution saturation state, *Am. J. Sci.*, *291*(7), 649–686.

Oelkers, E. H., and J. Schott (1995), Experimental study of anorthite dissolution and the relative mechanism of feldspar hydrolysis, *Geochim. Cosmochim. Acta*, *59*(24), 5039–5053.

Oh, W., and W. B. Lindquist (1999), Image thresholding by indicator kriging, *IEEE Trans. Pattern Anal. Mach. Intell.*, *21*(7), 590–602.

Patzek, T. W., (2001), Verification of a complete pore network simulator of drainage and imbibition, *SPE J.*, *6*, 155–156.

Peters, C. A. (2009), Accessibilities of reactive minerals in consolidated sedimentary rock: An imaging study of three sandstones, *Chem. Geol.*, *265*(1–2), 198–208.

Serra, J. (1982), *Image Analysis and Mathematical Morphology*, 610 pp., Academic, London.

Shin, H., W. B. Lindquist, D. L. Sahagian, and S. R. Song (2005), Analysis of the vesicular structure of basalts, *Comput. Geosci.*, *31*(4), 473–487.

Sholokova, Y., D. Kim, and W. B. Lindquist (2009), Network flow modeling via lattice-Boltzmann based channel conductance, *Adv. Water Resour.*, *32*(2), 205–212.

Steefel, C. I., and K. T. B. MacQuarrie (1996), Approaches to modeling of reactive transport in porous media, in *Reactive Transport in Porous Media*, edited by P. C. Lichtner, C. I. Steefel, and E. H. Oelkers, pp. 83–125, Mineral. Soc. of Am., Washington, D. C.

Trefethen, L. N., and D. Bau (1997), *Numerical Linear Algebra*, 361 pp., Society of Industrial and Applied Mathematics (SIAM), Philadelphia, Pa.